Applied Energy 228 (2018) 2333–2345

Contents lists available at ScienceDirect

Applied Energy

journal homepage: www.elsevier.com/locate/apenergy

Continuous adjoint formulation for wind farm layout optimization: A 2D implementation

Enrico G.A. Antonini*, David A. Romero, Cristina H. Amon

University of Toronto, Toronto, Canada

HIGHLIGHTS

- The developed adjoint method can effectively be used for WFLO gradient computations.
- The adjoint method significantly reduces the cost for the gradient computation.
- The AEP is improved on average by 15% with gradient-based layout optimization.

ARTICLE INFO

Keywords:
Wind farm layout optimization
CFD
RANS
Adjoint method
Gradient-based optimization

ABSTRACT

Current methodologies to optimize wind farm layouts to maximize the farm energy production rely on simple analytical models for wake loss estimations. In this paper, we present an innovative continuous adjoint formulation for gradient calculations within the framework of a gradient-based wind farm layout optimization. The developed optimization methodology integrates high-fidelity CFD models and, thanks to the adjoint method, overcomes the computationally high costs of a CFD-based optimization. The proposed continuous adjoint formulation allows for a derivation of the general adjoint equations, before any discretization is being applied, and therefore allows for a more flexible implementation in CFD software packages. Adjoint formulations for different conditions in the flow equations, namely, laminar, frozen-turbulence and turbulent flows are presented. The proposed formulation was implemented in a 2D domain and verified by comparing the calculated gradients with finite-difference approximations. Gradient calculations using the developed adjoint method were implemented in a gradient-based optimization methodology with open source software libraries, and were used to solve a 2D wind farm layout optimization problem under a wide array of wind resource scenarios. Our results showed that the annual energy production (AEP) of a given wind farm layout can be effectively improved within 30–60 iterations, depending on the initial layout and wind resource distribution. Improvements in AEP were found to be in the range of 7–37%, with an average of 15%.

1. Introduction

The wind farm layout optimization (WFLO) consists in finding the optimal spatial arrangement of wind turbines within a given wind farm terrain and boundary, typically to maximize the annual energy generated by the system. The WFLO has attracted a lot of attention from researchers and industry practitioners as it has been proven that better placement of wind turbines can increase the overall efficiency and the total revenue of a wind farm [1,2]. In addition, recent developments in optimization methodologies have started accounting for the health and environmental impact of wind farms, as it has become a matter of concern for governments and wind farm designers, particularly regarding noise generation, land use, and infrastructure deployment [3–5].

The main phenomenon that occurs in wind farms and affects their performance is the wake generated by the wind turbines. The wakes are regions of low wind speed that are the result of the kinetic energy extracted by the turbines. These wakes lower the speed of the wind entering the turbines placed downstream and, consequently, reduce their power production. In large wind farms, this effect has been shown to diminish the annual energy production by 10–20% [6]. The placement of wind turbines within a wind farm is hence a crucial factor, and an optimization process is strictly required to extract the maximum energy and minimize the cost of energy production.

From a design perspective, the WFLO problem requires therefore to accurately estimate the wake losses in wind farms. Different approaches

* Corresponding author.
E-mail address: enrico.antonini@mail.utoronto.ca (E.G.A. Antonini).

https://doi.org/10.1016/j.apenergy.2018.07.076
Received 12 April 2018; Received in revised form 21 June 2018; Accepted 14 July 2018
Available online 25 July 2018

exist to model wind turbine wakes, namely analytical and numerical models [7]. Analytical wake models are based on self-similar velocity deficit profiles obtained from experimental and theoretical work and have the advantage of being simple and computationally efficient. Among the most used analytical wake models are the ones developed by Jensen [8], Larsen [9], and Frandsen et al. [10]. These models are calibrated to a single turbine operating in isolation by means of empirical constants. Ad hoc models for wakes overlapping from multiple turbines need also to be introduced for wind farm power calculations [11,12]: they usually assume simple superimposition of turbine wakes and neglect the complex turbulent mixing occurring in wind farms. Because of these simplifications, the analytical wake models are not capable of accurately dealing with flow structures introduced by atmospheric conditions, changes in terrain roughness, speed-up effects around turbines or terrain features, and complex flow phenomena such as wake meandering [6].

On the other hand, numerical models, which rely on Computational Fluid Dynamics (CFD), offer higher accuracy and flexibility to handle different ambient conditions and terrain topography. CFD models are based on the solution of the Navier-Stokes (NS) equation and, depending on the method used to model turbulence, two categories can be identified: Reynolds-Averaged Navier-Stokes (RANS) and Large-Eddy Simulation (LES) methods [13]. RANS methods are based on a time-averaging procedure for the flow field solution and require additional turbulence modeling to close the system of equations. These methods have been widely used in wind farm simulations and have been shown to be a robust tool especially when estimations of the mean flow field and power output are desired. The reader can refer to Refs. [7,13–17] for comprehensive analyses and reviews of the RANS methods. LES methods are instead based on filtered NS equations: they resolve the large energy-containing eddies whereas they introduce mathematical models for smaller eddies that are strongly affected by molecular viscosity and dissipation. Applications and further details of wind farm LES can be found in Ref. [18].

Common approaches found in the WFLO literature have focused on minimizing turbine wake interactions based on simplified mathematical models of wake behavior, and relying on optimization metaheuristics to solve the non-linear, multi-objective, constrained WFLO problem [1,2,19]. Metaheuristics and stochastic optimization methods are currently the state of the art in solving the wind farm layout optimization problem. Implementations are found of genetic/evolutionary algorithms (e.g., [4,5,20–24]), particle swarm optimization algorithms (e.g., [25–29]), simulated annealing methods (e.g., [30]), and greedy algorithms (e.g., [31]). Mathematical programming approaches are also common in the WFLO: they are often implemented as stand-alone methods (e.g., [32–34]) and sometime combined with heuristic methods (e.g., [35]). Recently, non-linear mathematical programming that uses exact gradient information has showed great potential in tackling this problem. In particular, gradient-based methodologies using the exact derivatives of the objective function and constraints were demonstrated to outperform genetic algorithms in terms of solution quality and computational cost [36].

Optimization methodologies that are integrated with CFD models face practical limits in terms of computer requirements: optimization processes require a large number of evaluations, and each CFD evaluation will usually have a significant computational cost. The number of required evaluations strictly depends on the particular problem being solved as well as the optimization algorithm being used, but it scales with the number of optimization variables (i.e., the number of turines), and generally ranges from hundreds to hundreds of thousands evaluations. In the context of WFLO, the number of evaluations was lower when mathematical programming algorithms were used [36], and highest for metaheuristic methods [21,23]. A clear consequence is that a CFD-based optimization is only possible when the number of required evaluations is relatively low and, moreover, when the duration of a single CFD computation does not exceed a few hours at most [37]. These constraints have prevented the use of CFD models in the WFLO problem.

The first studies on the coupling of CFD models with optimization to tackle the WFLO problem have been recently conducted. Kuo et al. [38] proposed an algorithm that couples CFD with mixed-integer programming (MIP) to optimize layouts on complex terrains. Thanks to the proposed methodology, the study achieved a convenient trade-off between computational cost and solution quality. King et al. [39,40] developed a gradient-based approach to solve the WFLO problem which used an adjoint method in its discrete formulation. The adjoint method is a means to compute the gradient required by gradient-based optimization methods when the objective function depends on a set of state variables (for this case, the NS equations) [41]. Adjoint methods can generally be divided into discrete and continuous methods [37]. Their main characteristic is that the total cost for the gradient computation does not depend on the number of design variables but is approximately equal to that of a single CFD evaluation. Thanks to this feature, the adjoint methods have been widely and successfully used in aerodynamic shape optimization and geophysical tomography (e.g., [42–47]).

In the present paper, we describe an optimization methodology that integrates the high accuracy and flexibility offered by the CFD models and that overcomes the computationally high costs of a CFD-based optimization. To this end, we present an adjoint method in its continuous formulation for the gradient computation. To the authors' best knowledge, this is the first continuous formulation of the adjoint method applied to the gradient computation in the WFLO problem. The continuous adjoint formulation allows for a derivation of the general adjoint equations, before any discretization is being applied, and therefore allows also for a more flexible implementation in CFD software packages. Here we present a formulation for different conditions in the flow equations, namely, laminar, frozen-turbulence and turbulent flows. To verify the developed formulation, gradients calculated under these different flow conditions are compared with gradients computed with traditional central-difference schemes. The gradient calculation using the developed adjoint method is then incorporated into a gradient-based optimization methodology and applied to a set of 2D case studies with a wide variety of wind resource profiles.

2. The adjoint method

This section illustrates the general framework underlying the adjoint method, as first conceptualized by Jameson [42], and its computational advantages. Suppose that the governing equations of a system can be expressed as $\boldsymbol{G}(\boldsymbol{\phi}, \boldsymbol{\alpha}) = 0$, where $\boldsymbol{G}$ is the set of differential equations expressed in vector form (e.g., the RANS equations), $\boldsymbol{\phi}$ is the vector of state variables (e.g., the flow field variables), and $\boldsymbol{\alpha}$ is a vector of the design variables (e.g., the wind turbine coordinates). The system of the governing equations implicitly states that the state variables, $\boldsymbol{\phi}$, are function of the design variables, $\boldsymbol{\alpha}$. A scalar objective function that measures a quantity of interest (e.g., the total power/energy production of the wind farm) can be expressed as the integral of a user-defined function, $J[\boldsymbol{\phi}(\boldsymbol{\alpha}), \boldsymbol{\alpha}]$, over a certain volume, Ω_O. Optimization problems are formulated such that the optimal design variables need to be found within certain constraints to maximize the objective function, namely:

$$\begin{aligned} \max_{\boldsymbol{\alpha}} \quad & \int_{\Omega_O} J[\boldsymbol{\phi}(\boldsymbol{\alpha}), \boldsymbol{\alpha}] d\Omega, \\ \text{subject to} \quad & \boldsymbol{G}[\boldsymbol{\phi}(\boldsymbol{\alpha}), \boldsymbol{\alpha}] = 0 \quad \text{in } \Omega, \\ & k(\boldsymbol{\alpha}) = 0, \\ & h(\boldsymbol{\alpha}) \leqslant 0, \end{aligned} \tag{1}$$

where h and k are additional equality and inequality constraints on the design variables $\boldsymbol{\alpha}$, such as upper and lower bounds on a control input (e.g., wind farm site boundaries, wind turbines interspacing), and Ω is the entire domain over which the constraints are applied.

Gradient-based optimization algorithms require the gradient of the

objective function with respect to all of the control parameters, i.e., $d\left(\int_{\Omega_O} J d\Omega\right) \Big/ d\boldsymbol{\alpha}$. The derivation of this gradient with the adjoint method can be shown starting from the definition of the Lagrangian function:

$$L = \int_{\Omega_O} J d\Omega + \int_{\Omega} \hat{\boldsymbol{\phi}}^T \boldsymbol{G} d\Omega, \tag{2}$$

where $\hat{\boldsymbol{\phi}}$ is the vector of the Lagrange multipliers, also called adjoint variables. As $\boldsymbol{G}$ is everywhere zero by construction, the Lagrangian and its variation are always equal in value to the objective function and its variation (i.e., $L = J$ and $\delta L = \delta\left(\int_{\Omega_O} J d\Omega\right)$) while $\hat{\boldsymbol{\phi}}$ can be arbitrarily chosen. By applying the chain rule, the variation of the Lagrangian can be shown to be:

$$\begin{aligned}\delta L = &\frac{\partial}{\partial \boldsymbol{\alpha}}\left(\int_{\Omega_O} J d\Omega\right)\delta\boldsymbol{\alpha} + \frac{\partial}{\partial \boldsymbol{\alpha}}\left(\int_{\Omega} \hat{\boldsymbol{\phi}}^T \boldsymbol{G} d\Omega\right)\delta\boldsymbol{\alpha} \\ &+ \int_{\Omega_O}\left(\frac{\partial J}{\partial \boldsymbol{\phi}} + \hat{\boldsymbol{\phi}}^T \frac{\partial \boldsymbol{G}}{\partial \boldsymbol{\phi}}\right)\frac{d\boldsymbol{\phi}}{d\boldsymbol{\alpha}}\delta\boldsymbol{\alpha} d\Omega + \int_{\Omega\setminus\Omega_O}\left(\hat{\boldsymbol{\phi}}^T \frac{\partial \boldsymbol{G}}{\partial \boldsymbol{\phi}}\right)\frac{d\boldsymbol{\phi}}{d\boldsymbol{\alpha}}\delta\boldsymbol{\alpha} d\Omega.\end{aligned} \tag{3}$$

Since the objective function is typically a simple user-defined function, its partial derivatives with respect to the design variables, $\partial\left(\int_{\Omega_O} J d\Omega\right) \Big/ \partial\boldsymbol{\alpha}$, and state variables, $\partial J/\partial\boldsymbol{\phi}$, are straightforward to calculate numerically and analytically, respectively. The partial derivative of the constraints with respect to the design variables, $\partial(\int_{\Omega} \hat{\boldsymbol{\phi}}^T \boldsymbol{G} d\Omega) / \partial\boldsymbol{\alpha}$, is equal to zero whenever the state equations, $\boldsymbol{G}$, are and remain satisfied. However, this is not the case when volume source terms in the state equations are themselves a function of the design variables. In such cases, in the partial derivative, a term representing the source position shift needs to be defined and this creates an imbalance in the state equations that can be computed numerically. The partial derivative of the constraints with respect to the state variables, $\partial\boldsymbol{G}/\partial\boldsymbol{\phi}$, can be determined with classic derivation rules. Lastly, $d\boldsymbol{\phi}/d\boldsymbol{\alpha}$ is the most expensive term to compute for high-dimensional design and state spaces. In the adjoint approach, this last term is eliminated by choosing the adjoint variables such that:

$$\begin{aligned}&\tfrac{\partial J}{\partial \boldsymbol{\phi}} + \hat{\boldsymbol{\phi}}^T \tfrac{\partial \boldsymbol{G}}{\partial \boldsymbol{\phi}} = 0 \quad \text{in } \Omega_O, \\ &\hat{\boldsymbol{\phi}}^T \tfrac{\partial \boldsymbol{G}}{\partial \boldsymbol{\phi}} = 0 \quad \text{in } \Omega\setminus\Omega_O,\end{aligned} \tag{4}$$

These are called the adjoint equations and their solution usually requires a computational time that is comparable to the solution of the flow equations. With the values of the adjoint variables, it is therefore easy to calculate the total gradient needed for the optimization algorithm:

$$\frac{d}{d\boldsymbol{\alpha}}\left(\int_{\Omega_O} J d\Omega\right) = \frac{dL}{d\boldsymbol{\alpha}} = \frac{\partial}{\partial\boldsymbol{\alpha}}\left(\int_{\Omega_O} J d\Omega\right) + \frac{\partial}{\partial\boldsymbol{\alpha}}\left(\int_{\Omega} \hat{\boldsymbol{\phi}}^T \boldsymbol{G} d\Omega\right). \tag{5}$$

3. Continuous adjoint formulation for the wind farm layout optimization problem

The formulation of the adjoint method needs to be derived for every problem to which it is applied. Specifically, this requires the derivation and the calculation of the partial derivative terms highlighted in the previous section. The formulation of the adjoint method for the wind farm layout optimization problem starts with the definition of the design variables, $\boldsymbol{\alpha}$, which are the coordinates of the wind turbines within the wind farm:

$$\boldsymbol{\alpha} = [(x_1, x_2)_k] \quad k = 1, \ldots, K, \tag{6}$$

where K is the total number of wind turbines.

Each wind turbines is modeled as an actuator disk, which is characterized by a cylindrical volume, defined by the rotor swept area, where a distributed force, defined as axial momentum source, F, is applied. The actuator disk model offers a convenient trade-off between computational cost and accuracy: even if it does not provide a detailed description of the wind turbine geometry, it is able to adequately capture its wake effect for the intended application in wind farm simulations and optimization [48,49]. The axial force applied on the flow field as function of the reference wind speed is:

$$F = \frac{1}{2}\rho\frac{\pi D^2}{4} C_T U_{ref}^2, \tag{7}$$

where ρ is the air density, D is the rotor diameter, U_{ref} is the upstream wind speed, and C_T is the thrust coefficient, obtained from the thrust coefficient curve of the wind turbine at the specified U_{ref}. The power generated can be computed as the product of the axial force and the average velocity over the actuator disk volume V:

$$P = F\overline{v_n} = F\frac{1}{V}\int_V v_n d\Omega = f\int_V v_n d\Omega, \tag{8}$$

where $\overline{v_n}$ is the average normal velocity over the wind turbine rotor volume, V. Because of the 2-dimensional problem formulation, the actual wind turbine rotor volume is a rectangular prism with unit height and rectangular base whose width is equal to the rotor diameter.

The objective function for the WFLO is the annual energy production (AEP) of the wind farm, which is a function of both the wind farm layout and the wind resource. Without loss of generality, herein we present a simplified version of the problem in which the objective function is the total power produced by the wind turbines under a single wind state, i.e.:

$$P = \int_{\Omega_O} J d\Omega = \int_{\Omega_O} f_k v_n d\Omega, \tag{9}$$

where

$$\Omega_O = \sum_{k=1}^{K} V_k, \tag{10}$$

$$f_k \in V_k. \tag{11}$$

For WFLO, given the statistical distribution of wind speeds and directions, the formulation above (Eq. (9)) is the elemental building block required to calculate the expected AEP, as follows:

$$AEP = 8760 \sum_{s=1}^{S}\sum_{t=1}^{T} p_{s,t} P_{s,t}, \tag{12}$$

where S and T are the number of wind speed and direction bins, respectively, $p_{s,t}$ is the probability of occurrence for each wind speed and direction bin, and $P_{s,t}$ is the total power produced by the turbines, Eq. (9), for a given wind speed and direction.

The governing equations for the present WFLO are the Navier-Stokes equations (i.e., the continuity (C) and momentum (M) equations) for steady, incompressible flow, which in the context of the adjoint formulation are the constraints of the problem, $\boldsymbol{G}$:

$$C: \quad \frac{\partial v_i}{\partial x_i} = 0 \qquad \text{in } \Omega, \tag{13}$$

$$M_i: \begin{cases} v_j\frac{\partial v_i}{\partial x_j} + \frac{\partial p^*}{\partial x_i} - \frac{\partial}{\partial x_j}(2\nu_{eff} S_{ij}) = 0 & \text{in } \Omega - \Omega_O, \\ v_j\frac{\partial v_i}{\partial x_j} + \frac{\partial p^*}{\partial x_i} - \frac{\partial}{\partial x_j}(2\nu_{eff} S_{ij}) + f_{k,i} = 0 & \text{in } V_k \quad k = 1, \ldots, K, \end{cases} \tag{14}$$

where $v_{i,j}$ is the mean velocity component; p^* is the mean kinematic pressure (i.e., p/ρ); f_k is the constant source term generated by the k-th turbine (modeled as an actuator disk); i, j are indexes over the coordinate directions; S_{ij} is the mean rate-of-strain tensor, defined as:

$$S_{ij} = \frac{1}{2}\left(\frac{\partial v_i}{\partial x_j} + \frac{\partial v_j}{\partial x_i}\right); \tag{15}$$

and ν_{eff} is the effective viscosity, which for a laminar case is simply equal to the fluid kinematic viscosity, $\nu_{eff} = \nu = \mu/\rho$, and for turbulent flows is the sum of the fluid and turbulent viscosity, $\nu_{eff} = \nu + \nu_{turb}$. The turbulent viscosity is the result of the Boussinesq's hypothesis to model

the Reynolds stresses that arise after the Reynolds averaging operation. Turbulence modeling is required to calculate this viscosity and close the Navier-Stokes equations, and, consequently, more equations need to be considered as constraints of the problem. In the present formulation we adopted the $k-\omega$ turbulence model to close the RANS equation, but the current approach can similarly be extended to other one- and two-equation turbulence models. For the $k-\omega$ turbulence model, the turbulent viscosity is given by the ratio between the turbulence kinetic energy, k, and the specific dissipation rate, ω. The equations to calculate these two variables are the following:

$$T_1: \; v_j\frac{\partial k}{\partial x_j} - 2\frac{k}{\omega}S^2 + \beta^* k\omega - \frac{\partial}{\partial x_j}\left[\left(\nu + \sigma^*\frac{k}{\omega}\right)\frac{\partial k}{\partial x_j}\right] = 0 \quad \text{in } \Omega, \tag{16}$$

$$T_2: \; v_j\frac{\partial \omega}{\partial x_j} - 2\alpha S^2 + \beta\omega^2 - \frac{\partial}{\partial x_j}\left[\left(\nu + \sigma\frac{k}{\omega}\right)\frac{\partial \omega}{\partial x_j}\right] = 0 \quad \text{in } \Omega, \tag{17}$$

where α, β, β^*, σ, σ^* are empirical constants of the model, and S is the modulus of the mean rate-of-strain tensor, defined as:

$$S = \sqrt{S_{ij}S_{ij}}. \tag{18}$$

The state variables, also called field variables, $\boldsymbol{\phi}$, for this problem are therefore:

$$\boldsymbol{\phi} = \begin{cases} (p^*, v_i) & \text{Laminar case,} \\ (p^*, v_i, k, \omega) & \text{Turbulent case.} \end{cases} \tag{19}$$

The derivation of the adjoint formulation depends on the state equations that govern the original system and on the problem assumptions. Three cases can be identified for the adjoint formulation: laminar, turbulent, and frozen-turbulence cases. The first two cases are the results of the original laminar and turbulent equations respectively, whereas the latter is the results of turbulent equations when the frozen-turbulence hypothesis is used. Under this assumption, the variation of the turbulence field is neglected (i.e., the turbulent viscosity is assumed constant with respect to the mean velocities), and only changes of the mean flow are taken into account, described through the system for continuity and momentum. Although the gradient obtained by freezing the turbulence field is incomplete, this assumption is a convenient simplification that is considered standard for adjoint methods [50], and as such it is also adopted in the present work.

The Lagrangian function that results for the laminar and frozen-turbulence cases is:

$$L = \int_{\Omega_O} f_k v_n d\Omega + \int_{\Omega} (\hat{p}, \hat{v}_i)\cdot(C, M_i)d\Omega, \tag{20}$$

whereas for the turbulent case, the Lagrangian function is given by:

$$L = \int_{\Omega_O} f_k v_n d\Omega + \int_{\Omega} (\hat{p}, \hat{v}_i, \hat{k}, \hat{\omega})\cdot(C, M_i, T_1, T_2)d\Omega, \tag{21}$$

where the adjoint variables, $\hat{\boldsymbol{\phi}}$, for each of the cases are the following:

$$\hat{\boldsymbol{\phi}} = \begin{cases} (\hat{p}, \hat{v}_i) & \text{Laminar and frozen-turbulence cases,} \\ (\hat{p}, \hat{v}_i, \hat{k}, \hat{\omega}) & \text{Turbulent case.} \end{cases} \tag{22}$$

The derivation of the terms given in Eq. (3) and used to calculate the total gradient follows classical techniques from calculus of variations. The first terms analyzed here are the partial derivatives with respect to the design variables. As opposed to the traditional shape optimization formulations, the WFLO problem does not require surface sensitivities which would in turn require surface displacements and mesh deformation. In the current problem, the calculation of the wind turbine position sensitivities entails instead the displacements of the volumes where the source terms are applied without the need of mesh deformation. In fact, the source terms will be shifted over different regions depending of the chosen displacements to calculate the partial derivatives with respect to the design variables (see Fig. 1 for clarification purposes).

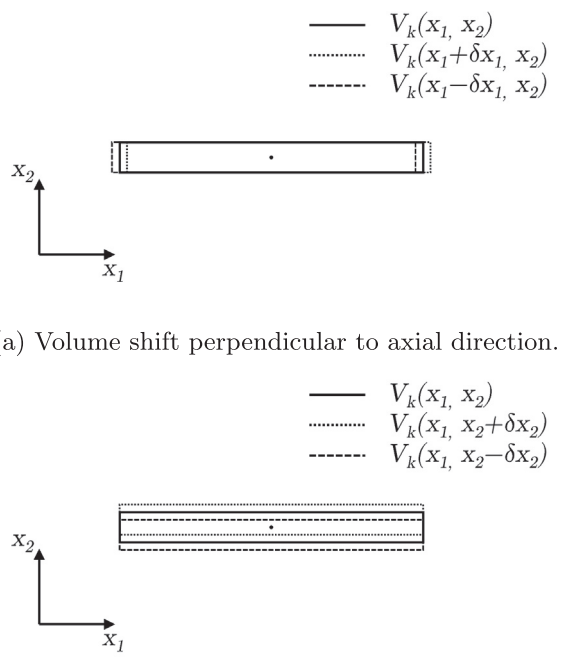

Fig. 1. Schematic illustrating the calculation of material partial derivatives.

When considering the partial derivative of the objective function, the resulting expression is the following:

$$\frac{\partial}{\partial \boldsymbol{\alpha}}\left(\int_{\Omega_O} J d\Omega\right) = \frac{\partial}{\partial \boldsymbol{\alpha}}\left(\int_{\Omega_O} f_k v_n d\Omega\right). \tag{23}$$

The calculation of this term requires the normal average velocity over the shifted volumes illustrated in Fig. 1 for each of the design variables. This can be computed numerically with a central difference discretization at no additional cost given that the field variables are already known:

$$\frac{\partial}{\partial \boldsymbol{\alpha}}\left(\int_{\Omega_O} J d\Omega\right) = \frac{\partial}{\partial[(x_1, x_2)_k]}\left(\int_{V_k} f_k v_n d\Omega\right) \quad k = 1, \ldots, K. \tag{24}$$

When considering instead the partial derivative of the augmented constraints, it can be seen that the displacements of the source terms affect only the momentum equations, whereas the other state equations remain equal to zero. The resulting expression is therefore the following:

$$\frac{\partial}{\partial \boldsymbol{\alpha}}\left(\int_{\Omega} \hat{\boldsymbol{\phi}}^T \boldsymbol{G} d\Omega\right) = \frac{\partial}{\partial \boldsymbol{\alpha}}\left(\int_{\Omega} \hat{v}_i \cdot M_i d\Omega\right). \tag{25}$$

If the state equations remained satisfied everywhere in Ω when calculating the partial derivative in Eq. (25), this term would result equal to zero. However, because the turbine (source term) positions are the design variables of the problem and their displacements need to be defined and applied to calculate the derivative, an imbalance in the momentum equations is created. This imbalance is equal to the source term and is present with a positive value in the regions where the shifted volumes do not overlap with the original turbine volume or with a negative value where the original volume does not overlap with shifted volumes. In formulas, this can be expressed as:

$$\frac{\partial}{\partial \boldsymbol{\alpha}}\left(\int_{\Omega} \hat{\boldsymbol{\phi}}^T \boldsymbol{G} d\Omega\right) = \frac{\partial}{\partial[(x_1, x_2)_k]}\left(\int_{V_{k,imb}} f_k \hat{v}_n d\Omega\right) \quad k = 1, \ldots, K, \tag{26}$$

where $V_{k,imb}$ refers to the region where the momentum equations result imbalanced when a central difference approximation is used to discretize the derivative and a volume shift is applied. The final result can be computed numerically once the adjoint variables are known.

The two partial derivatives calculated in Eqs. (25) and (26) are the fundamental components used to obtain the final value of the objective function gradient. However, other terms are needed to calculate the required adjoint variables. For this purpose, the last two terms given in Eq. (3), namely the partial derivatives with respect to the field variables, need to be calculated. First, the partial derivative of the objective function can be easily calculated as:

$$\int_{\Omega_O} \frac{\partial J}{\partial \boldsymbol{\phi}} \delta\boldsymbol{\phi} d\Omega = \int_{\Omega_O} \frac{\partial}{\partial \boldsymbol{\phi}} (f_k v_n) \delta v_n d\Omega = \int_{\Omega_O} f_{k,i} \delta v_i d\Omega. \tag{27}$$

The second term is the partial derivative of the augmented constraints and it requires instead a few algebraic manipulations to obtain a convenient relation that can be subsequently used for the adjoint equations. To derive it, the following rule for integration by parts for multivariable calculus will be used:

$$\int_\Omega \frac{\partial g}{\partial x_i} h d\Omega = \int_\Gamma g h n_i d\Gamma - \int_\Omega \frac{\partial h}{\partial x_i} g d\Omega. \tag{28}$$

Also, depending on the cases previously discussed (i.e., laminar, frozen-turbulence, and turbulent), different equation will be derived. The following sections will illustrate the two different derivations.

3.1. Adjoint equations for the laminar and frozen-turbulence cases

The adjoint equations and boundary conditions for the laminar and frozen-turbulence cases are derived by developing the last term required:

$$\begin{aligned}\int_\Omega \hat{\boldsymbol{\phi}}^T \frac{\partial \boldsymbol{G}}{\partial \boldsymbol{\phi}} \delta\boldsymbol{\phi} d\Omega = & \int_\Omega \hat{p} \left\{ -\frac{\partial \delta v_i}{\partial x_i} \right\} d\Omega \\ & + \int_\Omega \hat{v}_i \left\{ \delta v_j \frac{\partial v_i}{\partial x_j} + v_j \frac{\partial \delta v_i}{\partial x_j} + \frac{\partial \delta p^*}{\partial x_i} - \frac{\partial}{\partial x_j} (2\nu_{eff} \delta S_{ij}) \right\} d\Omega,\end{aligned} \tag{29}$$

where

$$\delta S_{ij} = \frac{1}{2} \left(\frac{\partial \delta v_i}{\partial x_j} + \frac{\partial \delta v_j}{\partial x_i} \right). \tag{30}$$

The integration by parts is used (twice for the diffusion term) to obtain the final expression:

$$\begin{aligned}\int_\Omega \hat{\boldsymbol{\phi}}^T \frac{\partial \boldsymbol{G}}{\partial \boldsymbol{\phi}} \delta\boldsymbol{\phi} d\Omega = & - \int_\Omega \left\{ -\frac{\partial \hat{p}}{\partial x_i} \delta v_i - \hat{v}_i \frac{\partial v_i}{\partial x_j} \delta v_j + v_j \frac{\partial \hat{v}_i}{\partial x_j} \delta v_i + \frac{\partial \hat{v}_i}{\partial x_i} \delta p^* \right. \\ & \left. + \frac{\partial}{\partial x_j} (2\nu_{eff} \hat{S}_{ij}) \delta v_i \right\} d\Omega \\ & + \int_\Gamma \{ -\hat{p} n_i \delta v_i + \hat{v}_i v_j n_j \delta v_i + \hat{v}_i n_i \delta p^* - \hat{v}_i 2\nu_{eff} \delta S_{ij} n_j \\ & + 2\nu_{eff} \hat{S}_{ij} n_j \delta v_i \} d\Gamma,\end{aligned} \tag{31}$$

where

$$\hat{S}_{ij} = \frac{1}{2} \left(\frac{\partial \hat{v}_i}{\partial x_j} + \frac{\partial \hat{v}_j}{\partial x_i} \right). \tag{32}$$

After collecting terms with the variations of the field variables, the resulting expression is the following:

$$\begin{aligned}\int_\Omega \hat{\boldsymbol{\phi}}^T \frac{\partial \boldsymbol{G}}{\partial \boldsymbol{\phi}} \delta\boldsymbol{\phi} d\Omega = & - \int_\Omega \left\{ \delta p^* \left[\frac{\partial \hat{v}_i}{\partial x_i} \right] + \delta v_i \left[v_j \frac{\partial \hat{v}_i}{\partial x_j} - \frac{\partial \hat{p}}{\partial x_i} - \hat{v}_j \frac{\partial v_j}{\partial x_i} \right. \right. \\ & \left. \left. + \frac{\partial}{\partial x_j} (2\nu_{eff} \hat{S}_{ij}) \right] \right\} d\Omega \\ & + \int_\Gamma \{ \delta p^* [\hat{v}_i n_i] + \delta v_i [\hat{v}_i v_j n_j - \hat{p} n_i + 2\nu_{eff} \hat{S}_{ij} n_j] \\ & - \hat{v}_i 2\nu_{eff} \delta S_{ij} n_j \} d\Gamma.\end{aligned} \tag{33}$$

The adjoint equations can be eventually determined to eliminate the variations of the field variables. By summing the partial derivatives of the objective function in Eq. (27) and of the augmented constraints in Eq. (33), the adjoint equations for the laminar and frozen-turbulence cases are:

$$\frac{\partial \hat{v}_i}{\partial x_i} = 0 \quad \text{in } \Omega, \tag{34}$$

$$\begin{cases} -v_j \frac{\partial \hat{v}_i}{\partial x_j} + \frac{\partial \hat{p}}{\partial x_i} - \frac{\partial}{\partial x_j} (2\nu_{eff} \hat{S}_{ij}) + \hat{v}_j \frac{\partial v_j}{\partial x_i} = 0 & \text{in } \Omega - \Omega_O, \\ -v_j \frac{\partial \hat{v}_i}{\partial x_j} + \frac{\partial \hat{p}}{\partial x_i} - \frac{\partial}{\partial x_j} (2\nu_{eff} \hat{S}_{ij}) + \hat{v}_j \frac{\partial v_j}{\partial x_i} + f_{k,i} = 0 & \text{in } V_k \ k = 1, \ldots, K, \end{cases} \tag{35}$$

$$\delta p^* [\hat{v}_i n_i] = 0 \quad \text{in } \Gamma, \tag{36}$$

$$\delta v_i [\hat{v}_i v_j n_j - \hat{p} n_i + 2\nu_{eff} \hat{S}_{ij} n_j] = 0 \quad \text{in } \Gamma, \tag{37}$$

$$\hat{v}_i 2\nu_{eff} \delta S_{ij} n_j = 0 \quad \text{in } \Gamma. \tag{38}$$

3.2. Adjoint equations for the turbulent case

The adjoint equations and boundary conditions for the turbulent case are derived, as in the previous case, by developing the last term required:

$$\begin{aligned}\int_\Omega \hat{\boldsymbol{\phi}}^T \frac{\partial \boldsymbol{G}}{\partial \boldsymbol{\phi}} \delta\boldsymbol{\phi} d\Omega = & \int_\Omega \hat{p} \left\{ -\frac{\partial \delta v_i}{\partial x_i} \right\} d\Omega \\ & + \int_\Omega \hat{v}_i \left\{ \delta v_j \frac{\partial v_i}{\partial x_j} + v_j \frac{\partial \delta v_i}{\partial x_j} + \frac{\partial \delta p^*}{\partial x_i} \right. \\ & \left. - \frac{\partial}{\partial x_j} \left[2 \left(\frac{\delta k}{\omega} - \frac{k}{\omega^2} \delta\omega \right) S_{ij} + 2 \left(\nu + \frac{k}{\omega} \right) \delta S_{ij} \right] \right\} d\Omega \\ & + \int_\Omega \hat{k} \left\{ \delta v_j \frac{\partial k}{\partial x_j} + v_j \frac{\partial \delta k}{\partial x_j} \right. \\ & - 2\frac{\delta k}{\omega} S^2 + 2\frac{k}{\omega^2} \delta\omega S^2 - 2\frac{k}{\omega} \delta(S^2) + \beta^* \delta k \omega + \beta^* k \delta\omega \\ & \left. - \frac{\partial}{\partial x_j} \left[\sigma^* \left(\frac{\delta k}{\omega} - \frac{k}{\omega^2} \delta\omega \right) \frac{\partial k}{\partial x_j} + \left(\nu + \sigma^* \frac{k}{\omega} \right) \frac{\partial \delta k}{\partial x_j} \right] \right\} d\Omega \\ & + \int_\Omega \hat{\omega} \left\{ \delta v_j \frac{\partial \omega}{\partial x_j} + v_j \frac{\partial \delta\omega}{\partial x_j} - 2\alpha\delta(S^2) + 2\beta\omega\delta\omega \right. \\ & \left. - \frac{\partial}{\partial x_j} \left[\sigma \left(\frac{\delta k}{\omega} - \frac{k}{\omega^2} \delta\omega \right) \frac{\partial \omega}{\partial x_j} + \left(\nu + \sigma \frac{k}{\omega} \right) \frac{\partial \delta\omega}{\partial x_j} \right] \right\} d\Omega,\end{aligned} \tag{39}$$

where

$$\delta(S^2) = 2 S_{ij} \frac{\partial \delta v_i}{\partial x_j}. \tag{40}$$

The integration by parts is used (twice for the diffusion term) to obtain the final expression:

$$
\begin{aligned}
\int_\Omega \hat{\boldsymbol{\phi}}^T \frac{\partial G}{\partial \boldsymbol{\phi}} d\Omega = -\int_\Omega \Big\{ & -\frac{\partial \hat{p}}{\partial x_i}\delta v_i \\
& - \hat{v}_i \frac{\partial v_i}{\partial x_j}\delta v_j + v_j \frac{\partial \hat{v}_i}{\partial x_j}\delta v_i + \frac{\partial \hat{v}_i}{\partial x_i}\delta p^* \\
& + \frac{\partial}{\partial x_j}\left[2\left(\nu + \frac{k}{\omega}\right)\hat{S}_{ij}\right]\delta v_i - \frac{\partial \hat{v}_i}{\partial x_j}\left[2\left(\frac{\delta k}{\omega} - \frac{k}{\omega^2}\delta\omega\right)S_{ij}\right] \\
& - \hat{k}\frac{\partial k}{\partial x_j}\delta v_j + v_j \frac{\partial \hat{k}}{\partial x_j}\delta k - \frac{\partial}{\partial x_j}\left(4\hat{k}\frac{k}{\omega}S_{ij}\right)\delta v_i \\
& - \hat{k}\left(-2\frac{S^2}{\omega}\delta k + 2\frac{k}{\omega^2}S^2\delta\omega + \beta^*\omega\delta k + \beta^* k\delta\omega\right) \\
& + \frac{\partial}{\partial x_j}\left[\left(\nu + \sigma^*\frac{k}{\omega}\right)\frac{\partial \hat{k}}{\partial x_j}\right]\delta k - \frac{\partial \hat{k}}{\partial x_j}\left[\sigma^*\left(\frac{\delta k}{\omega} - \frac{k}{\omega^2}\delta\omega\right)\frac{\partial k}{\partial x_j}\right] \\
& - \hat{\omega}\frac{\partial \omega}{\partial x_j}\delta v_j + v_j \frac{\partial \hat{\omega}}{\partial x_j}\delta\omega - \frac{\partial}{\partial x_j}(4\hat{\omega}\alpha S_{ij})\delta v_i - 2\beta\omega\hat{\omega}\delta\omega \\
& + \frac{\partial}{\partial x_j}\left[\left(\nu + \sigma\frac{k}{\omega}\right)\frac{\partial \hat{\omega}}{\partial x_j}\right]\delta\omega - \frac{\partial \hat{\omega}}{\partial x_j}\left[\sigma\left(\frac{\delta k}{\omega} - \frac{k}{\omega^2}\delta\omega\right)\frac{\partial \omega}{\partial x_j}\right]\Big\} d\Omega \\
& + \int_\Gamma \{ -\hat{p}\, n_i \delta v_i \\
& + \hat{v}_i v_j n_j \delta v_i + \hat{v}_i n_i \delta p^* \\
& - \hat{v}_i\left[2\left(\frac{\delta k}{\omega} - \frac{k}{\omega^2}\delta\omega\right)S_{ij} + 2\left(\nu + \frac{k}{\omega}\right)\delta S_{ij}\right]n_j \\
& + 2\left(\nu + \frac{k}{\omega}\right)\hat{S}_{ij} n_j \delta v_i \\
& + \hat{k} v_j n_j \delta k - 4\hat{k}\frac{k}{\omega}S_{ij} n_j \delta v_i \\
& - \hat{k}\left[\sigma^*\left(\frac{\delta k}{\omega} - \frac{k}{\omega^2}\delta\omega\right)\frac{\partial k}{\partial x_j} + \left(\nu + \sigma^*\frac{k}{\omega}\right)\frac{\partial \delta k}{\partial x_j}\right]n_j \\
& + \left(\nu + \sigma^*\frac{k}{\omega}\right)\frac{\partial \hat{k}}{\partial x_j} n_j \delta k \\
& + \hat{\omega} v_j n_j \delta\omega - 4\hat{\omega}\alpha S_{ij} n_j \delta v_i \\
& - \hat{\omega}\left[\sigma\left(\frac{\delta k}{\omega} - \frac{k}{\omega^2}\delta\omega\right)\frac{\partial \omega}{\partial x_j} + \left(\nu + \sigma^*\frac{k}{\omega}\right)\frac{\partial \delta\omega}{\partial x_j}\right]n_j \\
& + \left(\nu + \sigma\frac{k}{\omega}\right)\frac{\partial \hat{\omega}}{\partial x_j} n_j \delta\omega\Big\} d\Gamma.
\end{aligned}
\tag{41}
$$

After collecting terms with the variations of the field variables, the resulting expression is the following:

$$
\begin{aligned}
\int_\Omega \hat{\boldsymbol{\phi}}^T \frac{\partial G}{\partial \boldsymbol{\phi}} \delta\boldsymbol{\phi} d\Omega = -\int_\Omega \Big\{ & \delta p^* \left\{\frac{\partial \hat{v}_i}{\partial x_i}\right\} \\
& + \delta v_i \Big\{ v_j \frac{\partial \hat{v}_i}{\partial x_j} - \frac{\partial \hat{p}}{\partial x_i} - \hat{v}_j \frac{\partial v_j}{\partial x_i} - \hat{k}\frac{\partial k}{\partial x_i} - \hat{\omega}\frac{\partial \omega}{\partial x_i} \\
& + \frac{\partial}{\partial x_j}\left[2\left(\nu + \frac{k}{\omega}\right)\hat{S}_{ij}\right] - \frac{\partial}{\partial x_j}\left(4\hat{k}\frac{k}{\omega}S_{ij}\right) - \frac{\partial}{\partial x_j}(4\hat{\omega}\alpha S_{ij})\Big\} \\
& + \delta k \Big\{ v_j \frac{\partial \hat{k}}{\partial x_j} + \frac{\partial}{\partial x_j}\left[\left(\nu + \sigma^*\frac{k}{\omega}\right)\frac{\partial \hat{k}}{\partial x_j}\right] - \frac{1}{\omega}2S_{ij}\frac{\partial \hat{v}_i}{\partial x_j} \\
& - \frac{\sigma^*}{\omega}\frac{\partial k}{\partial x_j}\frac{\partial \hat{k}}{\partial x_j} - \frac{\sigma}{\omega}\frac{\partial \omega}{\partial x_j}\frac{\partial \hat{\omega}}{\partial x_j} + 2\frac{\hat{k}}{\omega}S^2 - \beta^*\hat{k}\omega\Big\} \\
& + \delta\omega \Big\{ v_j \frac{\partial \hat{\omega}}{\partial x_j} + \frac{\partial}{\partial x_j}\left[\left(\nu + \sigma\frac{k}{\omega}\right)\frac{\partial \hat{\omega}}{\partial x_j}\right] + \frac{k}{\omega^2}2S_{ij}\frac{\partial \hat{v}_i}{\partial x_j} \\
& + \frac{\sigma^* k}{\omega^2}\frac{\partial k}{\partial x_j}\frac{\partial \hat{k}}{\partial x_j} + \frac{\sigma k}{\omega^2}\frac{\partial \omega}{\partial x_j}\frac{\partial \hat{\omega}}{\partial x_j} - 2\frac{k\hat{k}}{\omega^2}S^2 - \beta^*\hat{k}k - 2\beta\hat{\omega}\omega\Big\}\Big\} d\Omega \\
& + \int_\Gamma \{\delta p^* [\hat{v}_i n_i] \\
& + \delta v_i \Big[\hat{v}_i v_j n_j - \hat{p}\, n_i + 2\left(\nu + \frac{k}{\omega}\right)\hat{S}_{ij} n_j \\
& - \left(4\hat{k}\frac{k}{\omega} + 4\hat{\omega}\alpha\right)S_{ij} n_j\Big] - \hat{v}_i 2\left(\nu + \frac{k}{\omega}\right)\delta S_{ij} n_j \\
& + \delta k \Big[\hat{k} v_j n_j + \left(\nu + \sigma^*\frac{k}{\omega}\right)\frac{\partial \hat{k}}{\partial x_j} n_j - \frac{\hat{v}_i}{\omega}S_{ij} n_j \\
& - \frac{\sigma^*\hat{k}}{\omega}\frac{\partial k}{\partial x_j} - \frac{\sigma\hat{\omega}}{\omega}\frac{\partial \omega}{\partial x_j}\Big] - \hat{k}\left(\nu + \sigma^*\frac{k}{\omega}\right)\frac{\partial \delta k}{\partial x_j} n_j \\
& + \delta\omega \Big[\hat{\omega} v_j n_j + \left(\nu + \sigma\frac{k}{\omega}\right)\frac{\partial \hat{\omega}}{\partial x_j} n_j + \frac{\hat{v}_i k}{\omega^2}S_{ij} n_j \\
& + \frac{\sigma^*\hat{k}k}{\omega^2}\frac{\partial k}{\partial x_j} + \frac{\sigma\hat{\omega}k}{\omega^2}\frac{\partial \omega}{\partial x_j}\Big] - \hat{\omega}\left(\nu + \sigma\frac{k}{\omega}\right)\frac{\partial \delta\omega}{\partial x_j} n_j\Big\} d\Gamma.
\end{aligned}
\tag{42}
$$

By eliminating the variations of the field variables and by summing the partial derivatives of the objective function in Eq. (27) and of the augmented constraints in Eq. (33), the adjoint equations for the turbulent case are:

$$
\frac{\partial \hat{v}_i}{\partial x_i} = 0 \qquad \text{in } \Omega, \tag{43}
$$

$$
\begin{cases}
-v_j\frac{\partial \hat{v}_i}{\partial x_j} + \frac{\partial \hat{p}}{\partial x_i} - \frac{\partial}{\partial x_j}\left[2\left(\nu + \frac{k}{\omega}\right)\hat{S}_{ij}\right] + \hat{v}_j\frac{\partial v_j}{\partial x_i} \\
\quad + \hat{k}\frac{\partial k}{\partial x_i} + \hat{\omega}\frac{\partial \omega}{\partial x_i} + \frac{\partial}{\partial x_j}\left[4\left(\hat{k}\frac{k}{\omega} + \alpha\hat{\omega}\right)S_{ij}\right] = 0 \qquad \text{in } \Omega - \Omega_O, \\
-v_j\frac{\partial \hat{v}_i}{\partial x_j} + \frac{\partial \hat{p}}{\partial x_i} - \frac{\partial}{\partial x_j}\left[2\left(\nu + \frac{k}{\omega}\right)\hat{S}_{ij}\right] + \hat{v}_j\frac{\partial v_j}{\partial x_i} \\
\quad + \hat{k}\frac{\partial k}{\partial x_i} + \hat{\omega}\frac{\partial \omega}{\partial x_i} + \frac{\partial}{\partial x_j}\left[4\left(\hat{k}\frac{k}{\omega} + \alpha\hat{\omega}\right)S_{ij}\right] + f_{k,i} \qquad \text{in } V_k \quad k = 1, \ldots, K, \\
\quad = 0
\end{cases}
\tag{44}
$$

$$
\begin{aligned}
& -v_j\frac{\partial \hat{k}}{\partial x_j} - \frac{\partial}{\partial x_j}\left[\left(\nu + \sigma^*\frac{k}{\omega}\right)\frac{\partial \hat{k}}{\partial x_j}\right] + \frac{1}{\omega}2S_{ij}\frac{\partial \hat{v}_i}{\partial x_j} \\
& \quad + \frac{\sigma^*}{\omega}\frac{\partial k}{\partial x_j}\frac{\partial \hat{k}}{\partial x_j} + \frac{\sigma}{\omega}\frac{\partial \omega}{\partial x_j}\frac{\partial \hat{\omega}}{\partial x_j} - 2\frac{\hat{k}}{\omega}S^2 + \beta^*\hat{k}\omega = 0 \qquad \text{in } \Omega,
\end{aligned}
\tag{45}
$$

$$
\begin{aligned}
& -v_j\frac{\partial \hat{\omega}}{\partial x_j} - \frac{\partial}{\partial x_j}\left[\left(\nu + \sigma\frac{k}{\omega}\right)\frac{\partial \hat{\omega}}{\partial x_j}\right] - \frac{k}{\omega^2}2S_{ij}\frac{\partial \hat{v}_i}{\partial x_j} \\
& \quad - \frac{\sigma^* k}{\omega^2}\frac{\partial k}{\partial x_j}\frac{\partial \hat{k}}{\partial x_j} - \frac{\sigma k}{\omega^2}\frac{\partial \omega}{\partial x_j}\frac{\partial \hat{\omega}}{\partial x_j} + 2\frac{k\hat{k}}{\omega^2}S^2 + \beta^*\hat{k}k + 2\beta\omega\hat{\omega} = 0 \qquad \text{in } \Omega,
\end{aligned}
\tag{46}
$$

$$
\delta p^* [\hat{v}_i n_i] = 0 \qquad \text{in } \Gamma, \tag{47}
$$

$$
\delta v_i\left[\hat{v}_i v_j n_j - \hat{p}\, n_i + 2\left(\nu + \frac{k}{\omega}\right)\hat{S}_{ij} n_j - 4\left(\hat{k}\frac{k}{\omega} + \hat{\omega}\alpha\right)S_{ij} n_j\right] = 0 \qquad \text{in } \Gamma, \tag{48}
$$

$$
\hat{v}_i 2\left(\nu + \frac{k}{\omega}\right)\delta S_{ij} n_j = 0 \qquad \text{in } \Gamma, \tag{49}
$$

$$
\delta k\left[\hat{k} v_j n_j + \left(\nu + \sigma^*\frac{k}{\omega}\right)\frac{\partial \hat{k}}{\partial x_j} n_j - \frac{\hat{v}_i}{\omega}S_{ij} n_j - \frac{\sigma^*\hat{k}}{\omega}\frac{\partial k}{\partial x_j} - \frac{\sigma\hat{\omega}}{\omega}\frac{\partial \omega}{\partial x_j}\right] = 0 \qquad \text{in } \Gamma, \tag{50}
$$

$$
\hat{k}\left(\nu + \sigma^*\frac{k}{\omega}\right)\frac{\partial \delta k}{\partial x_j} n_j = 0 \qquad \text{in } \Gamma, \tag{51}
$$

$$
\begin{aligned}
& \delta\omega\left[\hat{\omega} v_j n_j + \left(\nu + \sigma\frac{k}{\omega}\right)\frac{\partial \hat{\omega}}{\partial x_j} n_j + \frac{\hat{v}_i k}{\omega^2}S_{ij} n_j + \frac{\sigma^*\hat{k}k}{\omega^2}\frac{\partial k}{\partial x_j} + \frac{\sigma\hat{\omega}k}{\omega^2}\frac{\partial \omega}{\partial x_j}\right] \\
& \quad = 0 \qquad \text{in } \Gamma,
\end{aligned}
\tag{52}
$$

$$
\hat{\omega}\left(\nu + \sigma\frac{k}{\omega}\right)\frac{\partial \delta\omega}{\partial x_j} n_j = 0 \qquad \text{in } \Gamma. \tag{53}
$$

4. Verification

In this section, the verification of the proposed continuous adjoint method is carried out by comparing its results in terms of gradient computation with a finite difference discretization, defined according to:

$$
\frac{d}{d\boldsymbol{\alpha}}\left(\int_{\Omega_O} J d\Omega\right) = \frac{\int_{\Omega_O} J(\alpha_n + \delta\alpha_n) d\Omega - \int_{\Omega_O} J(\alpha_n - \delta\alpha_n) d\Omega}{2\delta\alpha_n} \quad n = 1, \ldots, N, \tag{54}
$$

where $\delta\alpha_n$ is a small variation of the n-th design variable. As opposed to the adjoint method, the gradient calculated with the central difference discretization requires two evaluations of the objective function, J, for each of the design variables. This form of verification has been extensively used in literature to assess the accuracy of the derivatives (e.g., [43,45,50,51]). It is important to note that, although the continuous adjoint formulation calculates the exact gradient, its

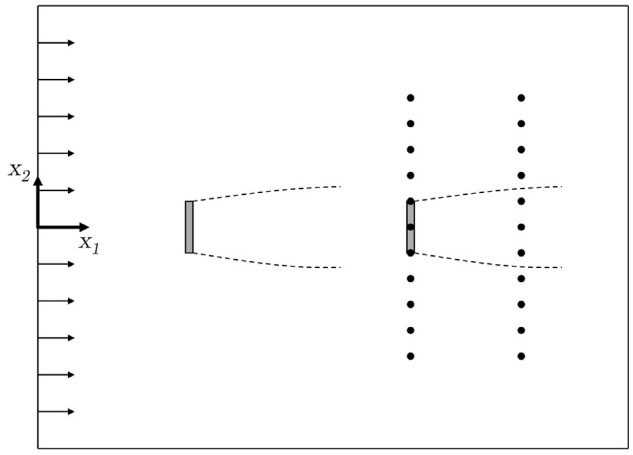

Fig. 2. Schematic of the layout for the verification case. The two grey areas represent the volumes where the wind turbine momentum sources are applied. The black dots indicate the different positions where the second wind turbine is placed when the gradient is calculated.

implementation requires the discretization of the equations over the same computational mesh of the primal simulation. Hence, both the central difference and adjoint method results are approximations to the underlying gradient, for which there are no closed-form expressions available.

The continuous adjoint method was therefore applied to the verification case shown in Fig. 2, which consists in finding the gradient of the power production of a turbine placed in the wake of another with respect to its turbine coordinates. For this case, a 2D domain was used and the results were obtained for the three formulations of the adjoint equations. To have a robust verification and to capture both streamwise and cross-wise variations, the gradient components were calculated for the two directions of the domain and on a regular grid of downstream and cross-stream positions. The downstream positions were set to $10D$ and $15D$, with a cross-stream spacing of $0.5D$, where D is the turbine rotor diameter equal to 80 m. These specific positions were chosen based on preliminary tests we performed to capture the largest variations in the calculated gradients.

The mathematical formulation of this adjoint problem was implemented in OpenFOAM [52]. The implementation took advantage of the top-level syntax of the code, which is very close to the conventional mathematical notation for tensors and partial differential equations [53]. Thanks to the high degree of similarity between the state and the adjoint equations, the latter ones were elegantly coded in a similar way to the NS equations. Second-order discretization was subsequently applied to the adjoint equations for the interpolation of the adjoint variables. Similarly to the NS equations, the semi-implicit method for pressure-linked equations (SIMPLE) algorithms was used to solve simultaneously the set of adjoint equations by an iterative scheme.

4.1. Boundary conditions

The boundary conditions for the wind turbines simulation were set with realistic values for wind speed and turbulence quantities. Even though the simulated system is 2-dimensional, an atmospheric boundary layer (ABL) was assumed to be present at the inlet. The relations that govern an ABL can be found in Ref. [16]. Given the ABL characterizing parameters, i.e., undisturbed speed at reference height, $U_{ref} = 10$ m/s, reference height, $H = 60$ m, and surface roughness, $z_0 = 0.0018$ m, the turbulence kinetic energy and specific dissipation rate were calculated and then prescribed at the inlet along with the wind speed. The outlet boundary condition was defined as pressure outlet, with zero gradient for the velocity and turbulence quantities. The side boundary condition was defined as zero gradient for all the variables.

With regards to the adjoint simulation, the definition of the boundary conditions requires a specific discussion. In traditional cases of shape design optimization, the boundaries of the domain are subject to variation depending on the design variables. Therefore the variation of the boundaries and the definition of the adjoint boundary conditions are crucial for an accurate gradient calculation (see Ref. [54] for a detailed analysis). In the present WFLO problem, the boundaries are not subject to any variation and they do not carry any objective function. Because of these circumstances, their influence on the gradient calculation was seen to be negligible. The boundary conditions on Γ for the present problem can therefore be fulfilled by the following solution:

$$\begin{aligned} &\hat{v_i} = 0 \quad \text{in } \Gamma, \\ &\tfrac{\partial \hat{p}}{\partial x_i} = 0 \quad \text{in } \Gamma, \\ &\hat{k} = 0 \quad \text{in } \Gamma, \\ &\hat{\omega} = 0 \quad \text{in } \Gamma. \end{aligned} \tag{55}$$

This solution enabled a straightforward implementation, a stable convergence of the iterative scheme, and accurate results when considering the gradient calculation.

4.2. Verification results

The results of the developed adjoint formulation were compared to those of a central difference (CD) approach, which can be considered as the best achievable solution for numerical gradient computations. Figs. 3 and 4 show the values of the gradient obtained by the three different adjoint formulations and the CD approach. Tables 1–3 report evaluation metrics when comparing the adjoint formulations and the CD approach. These are the relative magnitude of the gradient computed with the adjoint method:

$$\|\nabla J_{rel}\| = \frac{\|\nabla J_{AM}\|}{\|\nabla J_{AM,max}\|} \cdot 100; \tag{56}$$

the percentage difference in the absolute value of the gradients computed by the adjoint method with respect to the central difference approach:

$$\text{err}_{\nabla J} = \frac{\|\nabla J_{AM}\| - \|\nabla J_{CD}\|}{\|\nabla J_{CD,max}\|} \cdot 100; \tag{57}$$

the angular difference in the direction between the gradient calculated with the adjoint method and the central difference approach, according to:

$$\text{err}_{\theta} = \|\theta_{AM} - \theta_{CD}\|. \tag{58}$$

For the laminar case, the adjoint method could capture almost exactly the gradient given by the central difference approach for all the downstream positions. A maximum difference of 1.2% in the absolute value and a maximum difference of 1.5° in the direction were observed. When the frozen-turbulence assumption was used for the turbulence equations, higher discrepancies were seen between the results of the two methods, with a maximum difference of 12.0% in absolute value and a maximum difference of 72.3° in the direction. The fully turbulent formulation of the adjoint method had results that overall were comparable to the laminar case in terms of accuracy both in the absolute value and direction. However, for both the frozen-turbulence and turbulent results, high discrepancies were observed in the direction values for the cases where the second turbine was in the outermost lateral positions (2.0 and $2.5D$ cross-stream positions). This is related to the fact that the two components of the gradient approach a value of zero, and the direction of the gradient reported in the tables is calculated as the arctangent of a division of two small numbers, thus subject to numerical errors. As a result, small differences in the gradient components can show as large differences in its direction. However, this happens only when the magnitude of the gradient is significantly lower and

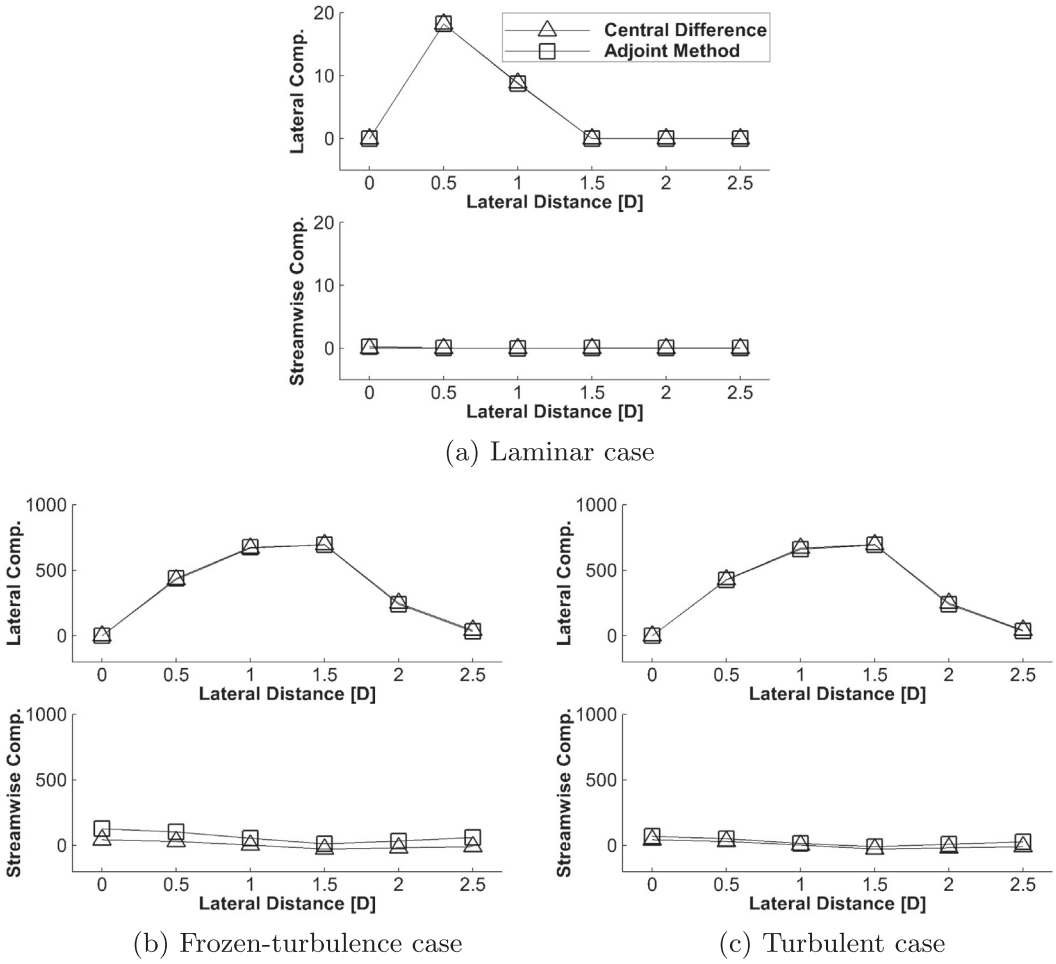

Fig. 3. Gradient computation required for a gradient-based optimization algorithm. The figures show the results obtained by the adjoint method compared to a central difference discretization approach for the different lateral positions of the second wind turbine at 10*D* downstream.

almost negligible with respect to the wake region. Therefore this behavior is not expected to affect the optimization process.

In terms of computational cost, the central difference approach required 4 simulations to compute the gradient. However, CD requires in general 2*N* system solutions, where *N* is the number of design variables (in the WFLO, there are two design variables per wind turbine). Instead, the adjoint method required the solution of the adjoint system and 4 numerical integrations (with negligible computational cost) to compute the gradient, regardless of the number of design variables. For the present verification case where the gradient of only one turbine was calculated, the computational cost of the adjoint method was 75% lower than the central difference approach. Higher reductions are however expected when more wind turbines are considered, such as the application case in the following section.

Overall, the results presented for this verification case showed that the adjoint method can effectively replace a traditional central difference approach for gradient computation and significantly reduce the amount of time required for the process. The adjoint method will be therefore integrated, in place of a central difference discretization, in the gradient-based optimization methodology illustrated in the following section.

5. Optimization methodology for the WFLO problem

The gradient calculation performed with the adjoint method is an essential component of the optimization methodology, which aims to find the optimal placement of a given number of wind turbines within a wind farm domain to maximize the AEP. The optimization methodology, illustrated in Fig. 5, starts with the wind rose, i.e., the site-specific statistical distribution of the wind resource, and an initial wind farm layout. Initially, CFD simulations are used to calculate the AEP of that particular configuration. If convergence/termination criteria in the iterative loop are not met, adjoint CFD simulations are then used to calculate the gradient of the objective function, i.e., the gradient of the AEP with respect to the turbine positions. Using the calculated gradients, turbine positions are updated to create a new turbine layout, which is then evaluated with a CFD simulation. These steps are repeated until convergence/termination criteria are met.

This methodology was entirely developed and implemented to run autonomously. Two separate routines were coded to take care of the calculation of the AEP and of the gradient. In these routines, the original and adjoint CFD simulations are automatically set up and run using OpenFOAM, and the results of interest are generated and passed to the rest of the loop. The overall optimization process, which consists of running the two aforementioned routines, updating the turbine position, and monitoring the convergence, is handled by a sequential quadratic programming (SQP) algorithm as implemented in the open-source library NLopt [55,56]. A stopping criterion is applied so that the optimization run is stopped when changes in the objective function from one iteration to the next are less than 0.01%.

The developed optimization methodology was applied to optimize a 2D wind farm layout consisting of 16 wind turbines using the fully turbulent formulation. The domain used for the CFD and adjoint simulations had a dimension of $40D \times 40D$, whereas the wind turbines

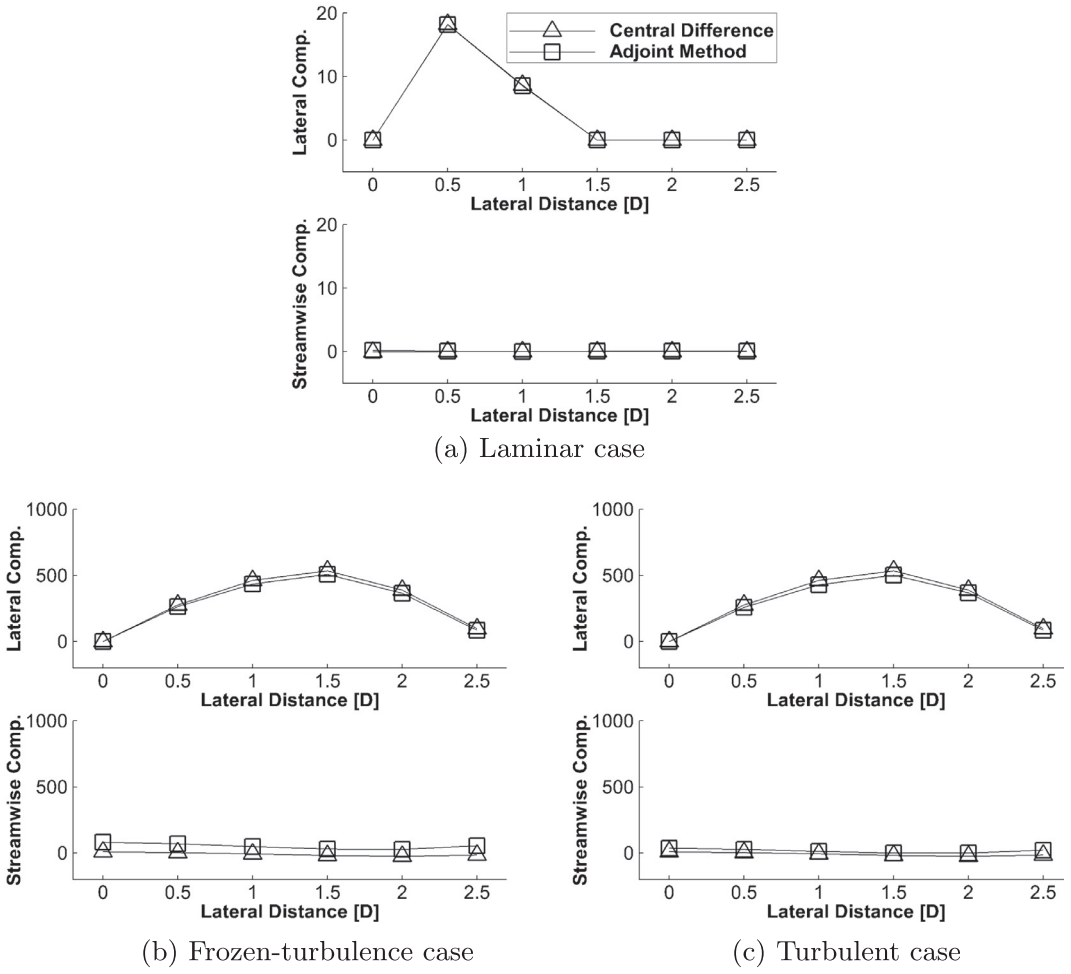

Fig. 4. Gradient computation required for a gradient-based optimization algorithm. The figures show the results obtained by the adjoint method compared to a central difference discretization approach for the different positions of the second wind turbine at 15D downstream.

Table 1
Relative magnitude of the gradient computed with the adjoint method, $\|\nabla J_{rel}\|$, and errors in magnitude, $\text{err}_{\nabla J}$, and direction, err_{θ}, between the gradient calculated with the adjoint method and the central difference approach on a grid of locations downstream of the turbine for the laminar case.

	10D downstream			15D downstream		
Cross-stream [D]	$\|\nabla J_{rel}\|$ [%]	$\text{err}_{\nabla J}$ [%]	err_{θ} [°]	$\|\nabla J_{rel}\|$ [%]	$\text{err}_{\nabla J}$ [%]	err_{θ} [°]
0.0	1.2	1.2	0.0	1.0	0.8	0.0
0.5	100.0	0.1	0.3	99.7	0.5	0.3
1.0	47.8	0.7	0.1	46.8	0.9	0.0
1.5	0.4	0.4	1.1	0.3	0.1	0.9
2.0	0.4	0.3	1.3	0.3	0.1	1.1
2.5	0.4	0.3	1.5	0.3	0.1	1.4

Table 2
Relative magnitude of the gradient computed with the adjoint method, $\|\nabla J_{rel}\|$, and errors in magnitude, $\text{err}_{\nabla J}$, and direction, err_{θ}, between the gradient calculated with the adjoint method and the central difference approach on a grid of locations downstream of the turbine for the frozen-turbulence case.

	10D downstream			15D downstream		
Cross-stream [D]	$\|\nabla J_{rel}\|$ [%]	$\text{err}_{\nabla J}$ [%]	err_{θ} [°]	$\|\nabla J_{rel}\|$ [%]	$\text{err}_{\nabla J}$ [%]	err_{θ} [°]
0.0	18.4	12.0	0.0	11.8	10.5	0.0
0.5	65.1	3.0	9.2	39.4	0.6	14.3
1.0	97.6	1.1	4.5	63.2	3.5	7.2
1.5	100.0	0.5	3.2	73.4	3.7	5.4
2.0	37.8	1.1	12.0	52.7	3.6	7.5
2.5	10.1	3.7	72.3	14.5	0.1	40.3

were constrained to be within a 17D-radius circumference, as shown in Fig. 6. This circular sub-domain was introduced as a computational convenience, to allow us to efficiently rotate the wind farm layout depending on the specified wind direction, rather than rotating the boundary conditions. A minimum distance of 1D between wind turbines was set as additional constraint to avoid any overlap of wind turbines generated by the optimization algorithm.

The convergence behavior of gradient-based optimization methods is highly dependent on the starting design configuration. Due to the local character of gradient information, gradient-based optimization methods are only guaranteed to perform local optimization, i.e., they converge to the nearest locally optimal solution, but they cannot guarantee that the global optimal solution is found. To overcome this limitation, the initial solution should be located in the basin of attraction of a global optimum to get a global optimum solution. Because of that, and to analyze the dependence of the gradient-based methodology to the initial configuration, two initial layouts were tested, namely a regular layout (commonly used in wind farms) and a random layout (see Fig. 7). With these initial layouts, seven different wind roses were chosen to conduct a comprehensive analysis of the proposed methodology. Six of these wind roses were composed of evenly weighted wind directions, whereas the last one was representative of a more realistic

Table 3
Relative magnitude of the gradient computed with the adjoint method, $\|\nabla J_{rel}\|$, and errors in magnitude, $err_{\nabla J}$, and direction, err_{θ}, between the gradient calculated with the adjoint method and the central difference approach on a grid of locations downstream of the turbine for the turbulent case.

	10*D* downstream			15*D* downstream		
Cross-stream [*D*]	$\|\nabla J_{rel}\|$ [%]	$err_{\nabla J}$ [%]	err_{θ} [°]	$\|\nabla J_{rel}\|$ [%]	$err_{\nabla J}$ [%]	err_{θ} [°]
0.0	9.9	3.6	0.0	5.1	3.9	0.0
0.5	62.0	0.1	2.8	37.6	2.4	5.3
1.0	95.1	1.2	1.3	62.1	4.5	2.5
1.5	100.0	0.5	1.3	72.6	4.6	2.0
2.0	34.6	1.4	6.0	53.0	3.4	3.6
2.5	6.6	0.2	47.8	12.7	1.7	22.2

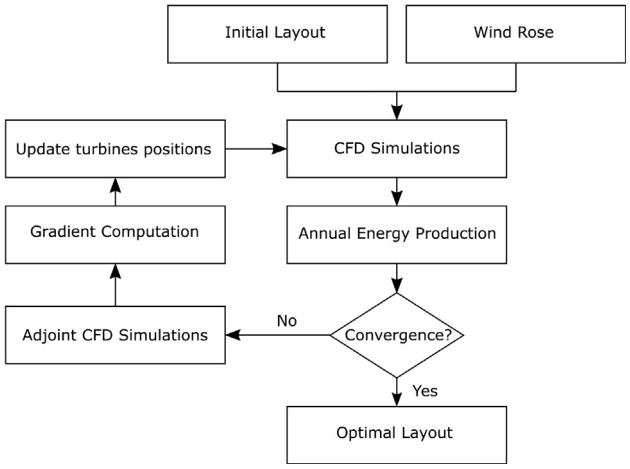

Fig. 5. Flow chart reproducing the optimization methodology used to solve the wind farm layout optimization problem

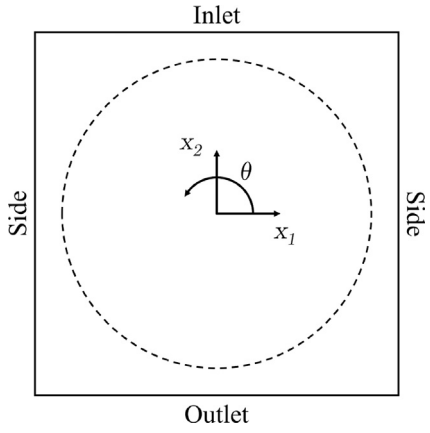

Fig. 6. Schematic of the 2D domain used to test the optimization methodology.

scenario with a predominant wind direction (see Figs. 8 and 9). For all wind resource distributions, the wind speed was considered constant at 10 m/s.

The results obtained from the optimization are reported in Figs. 8 and 9 for a regular and a random initial layout, respectively. For each wind rose reported on the left, the final optimal layout is shown in the center along with the value of the normalized AEP through the iterations on the right. The normalized AEP is defined as the ratio between the actual AEP and the AEP that would be generated by the same turbines operating in isolation. Convergence was reached in approximately 30–60 iterations of the optimization loop for all the cased analyzed. The results of the optimization process in terms of normalized AEP are

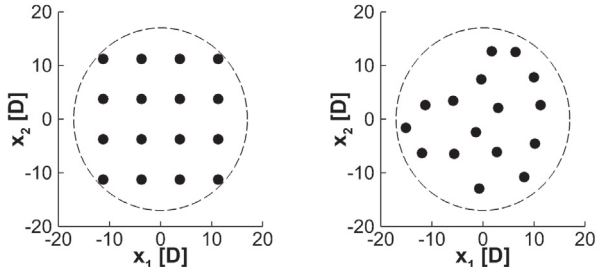

Fig. 7. Initial layouts used as inputs for the optimization process.

reported in Table 4.

For the cases with a regular initial layout, it is possible to notice that for evenly weighted wind roses the generated optimal layout retained a certain degree of regularity. For example, the layouts for 4 and 12 directions were symmetric about a 90° rotation; the layouts for 2 and 6 directions were instead symmetric about a horizontal or vertical line passing by the center of the domain. These characteristics of symmetry of the layouts for evenly weighted wind directions and for uniform wind speed are usually considered an indication of an effective optimization algorithm. Obviously, these characteristics of regularity could not be seen in the optimal layouts for other case of a random initial layout.

Looking at the results in terms of normalized AEP for the optimal layouts, it is interesting to notice that the actual AEP was greater, up to a maximum of 8%, than the one that would be generated by the same turbines operating in isolation. The reason for this interesting result can be explained by looking at two different aspects. First, the CFD simulations allow to accurately resolve the flow field and to capture the real behavior of wakes. In fact, besides creating a wind speed reduction in the wake of wind turbines, wakes also generate a local speed-up effect just outside of the wake region to compensate the wind speed deficit within the wake. The optimization algorithm took advantage of this flow characteristic and, depending on the wind rose, tried to move the wind turbines toward these favorable positions where the speedups were higher. This speedup effect is more pronounced in 2D simulations like the ones conducted in the present study, whereas its effect should be lower in 3D simulations [40]. Second, the wind farm had a low density because it consisted only of 16 wind turbines that could be spread over a wide area. This fact allowed the optimization algorithms to find favorable locations with speed-up effects for almost all the turbines. If the wind farm have had a higher wind turbine density, it is unlikely that the normalized AEP would have had a value greater than 1 because of the higher wake losses. It is also possible to notice that as the wind roses became less sparse, the maximum normalized AEP dropped from 1.07–1.08 for both the unidirectional wind roses to 1.00–1.01 for the 12-direction wind roses. This indicates that as the wind rose has more wind directions, it is more difficult to find favorable positions with speed-up effects for all the wind turbines and some of them end up in locations of partial wake shading.

With regards to the convergence behavior of the optimization algorithm, the results show that, as expected, the optimal layouts found with the proposed methodology were highly dependent on the initial layout. The optimal layouts obtained starting from a regular layout were very different from those obtained when the optimization started from a random layout. In terms of AEP, it was observed that the optimal layouts obtained when a regular layout was used as a starting point resulted in lower energy than those obtained starting from a random layout. In both cases, the algorithm can be said to have converged to a local minima, though the minimum of the objective function was lower in the random layout case. Another interesting observation that can be made from the results is that, for a regular initial layout and when the wind rose had directions aligned with the wind turbine arrangement (2-

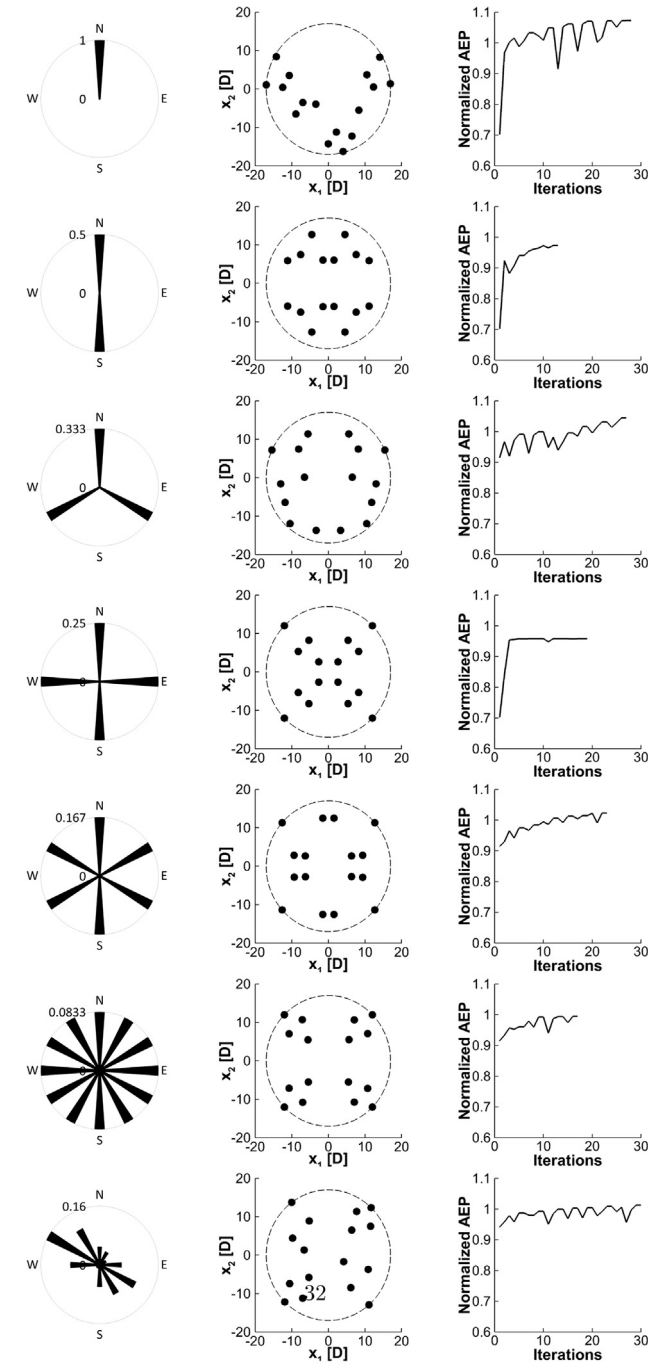

Fig. 8. Optimization results obtained from a regular initial layout. For each wind rose on the left, the final optimal layout is shown in the center along with the value of the normalized annual energy production (AEP) through the iterations on the right.

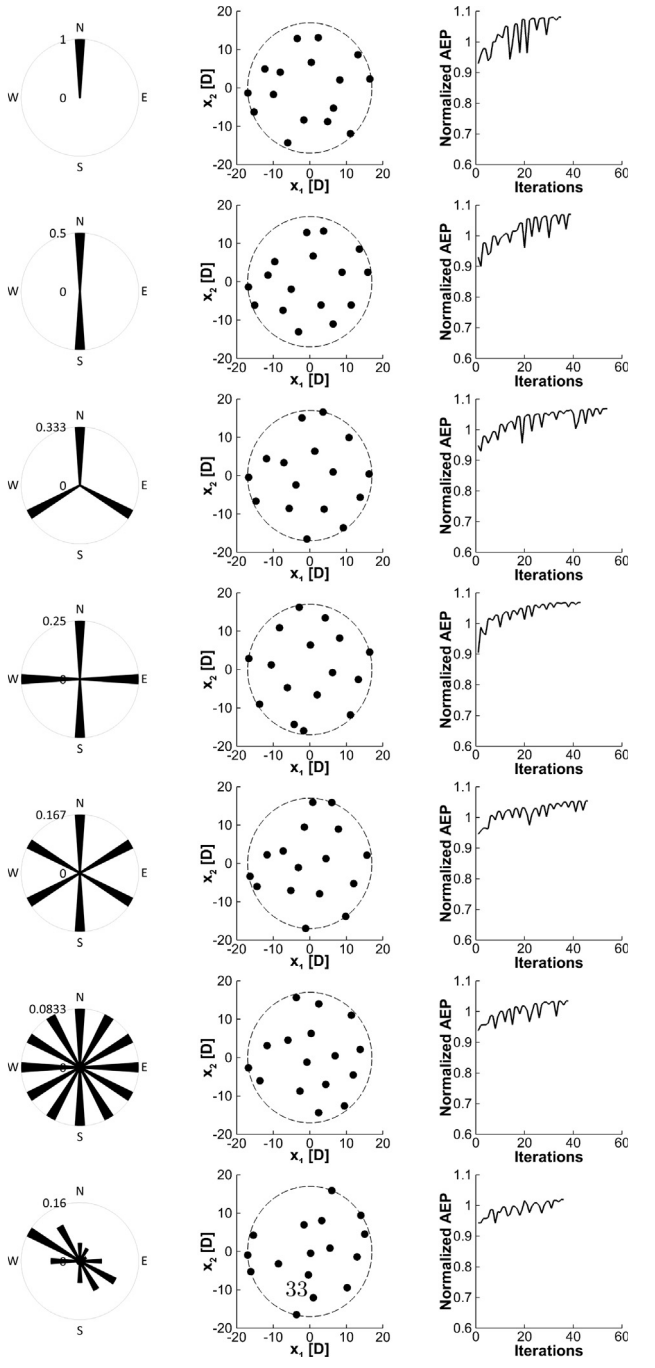

Fig. 9. Optimization results obtained from a random initial layout. For each wind rose on the left, the final optimal layout is shown in the center along with the value of the normalized annual energy production (AEP) through the iterations on the right.

and 4-direction wind roses), the optimization algorithm seemed to be trapped in a local optimum in the early stages of the optimization loop. This issue was not observed when the optimizations started from a random initial layout. This is evidence of the non-linear nature of the optimization problem, with strong interactions between the wind resource profile and the wind turbine layout.

Overall, the developed optimization methodology based on the adjoint method for the gradient computation could effectively improve the AEP of a given wind farm layout by changing its turbine positions. The improvements ranged from about 7% for the case of a 12-direction non-uniform wind rose and regular initial layout, to 37% for the case of a unidirectional wind rose and regular initial layout. On average, the improvements were of 18% and 12% for the regular and random initial layouts, respectively.

6. Conclusions

In the present paper, we developed an optimization methodology for the WFLO problem that integrates the high accuracy and flexibility offered by the CFD models and that overcomes the computationally high costs of a CFD-based optimization. To this end, we developed and used an adjoint method in its continuous formulation for the gradient computation. The adjoint formulation was derived for three different

Table 4
Normalized AEP and improvement with respect to the initial configuration obtained at the end of the optimization for each of the initial wind farm layouts and for each of the wind roses (WR) used.

	Regular initial layout		Random initial layout	
	Norm. AEP	Impr. [%]	Norm. AEP	Impr. [%]
1-dir. uniform WR	1.073	37.1	1.080	15.0
2-dir. uniform WR	0.973	27.1	1.070	13.9
3-dir. uniform WR	1.045	12.9	1.069	12.1
4-dir. uniform WR	0.958	25.6	1.069	16.4
6-dir. uniform WR	1.023	10.8	1.053	10.8
12-dir. uniform WR	0.995	8.0	1.034	9.6
12-dir. non-uniform WR	1.013	7.1	1.019	7.6

flow scenarios, namely, laminar, frozen-turbulence, and turbulent flows. The derived adjoint equations were implemented in OpenFOAM by taking advantage of the top-level syntax of the code and of the similarity between the Navier-Stokes and adjoint equations. The gradient calculation using the developed adjoint method was implemented in a gradient-based optimization methodology to solve a 2D WFLO problem.

The developed adjoint formulation was first verified on a simplified 2D 2-turbine wind farm where only the gradient of the wind turbine operating in wake conditions was considered. The results obtained with adjoint method in terms of gradient computations were generally accurate when compared to the results obtained with a central difference discretization. The calculated gradients showed higher accuracy for laminar and turbulent flow regimes, while lower accuracy was observed for the frozen-turbulence case. Overall, the results showed that the adjoint method could effectively replace a traditional central difference approach for gradient computation and significantly reduce the amount of time required for the process.

The gradient calculation performed with the adjoint method was implemented in an optimization methodology to solve a 2D WFLO problem. A hypothetical 16-turbine wind farm was defined with two different initial layouts, with turbine positions either set on a regular grid or random. Seven wind roses were also defined as inputs for the optimization for a comprehensive analysis. Six of them were formed by evenly weighted wind directions and one with a realistic wind rose with a predominant wind direction. The optimization methodology could effectively improve the AEP of the given wind farm layouts by changing the turbine positions on average by 18% and 12% for the regular and random initial layouts, respectively.

Overall, the developed continuous adjoint formulation and its results showed that significant improvements can be achieved in terms of computational time with respect to traditional approaches for gradient computation, such as the central difference approach, without diminishing the accuracy. The developed gradient-based optimization methodology using the adjoint method showed instead that it is possible to effectively improve the wind farm AEP. The optimization methodology showed also to benefit from the use of CFD models which offer a more detailed representation of the flow field in wind farms by, for example, capturing speed-up effects just outside of wake regions that cannot be observed with analytical wake models. This continuous adjoint formulation applied to a 2D WFLO is a first step toward a more general 3D formulation that could enable an optimization of wind farm layouts in complex terrain.

Acknowledgments

Computations were performed on the GPC (General Purpose Cluster) supercomputer at the SciNet HPC Consortium [57]. SciNet is funded by: the Canada Foundation for Innovation under the auspices of Compute Canada; the Government of Ontario; Ontario Research Fund - Research Excellence; and the University of Toronto.

References

[1] Herbert-Acero JF, Probst O, Réthoré P-E, Larsen GC, Castillo-Villar KK. A review of methodological approaches for the design and optimization of wind farms. Energies 2014;7(11):6930–7016. https://doi.org/10.3390/en7116930.
[2] Serrano González J, Burgos Payán M, Riquelme Santos JM, González-Longatt F. A review and recent developments in the optimal wind-turbine micro-siting problem. Renew Sustain Energy Rev 2014;30:133–44. https://doi.org/10.1016/j.rser.2013.09.027.
[3] Saidur R, Rahim NA, Islam MR, Solangi KH. Environmental impact of wind energy. Renew Sustain Energy Rev 2011;15(5):2423–30. https://doi.org/10.1016/j.rser.2011.02.024.
[4] Yin Kwong W, Zhang PY, Romero DA, Moran J, Morgenroth M, Amon CH. Multi-objective wind farm layout optimization considering energy generation and noise propagation with NSGA-II. J Mech Des 2014;136(9):091010. https://doi.org/10.1115/1.4027847.
[5] Yamani Douzi Sorkhabi S, Romero DA, Yan GK, Gu MD, Moran J, Morgenroth M, et al. The impact of land use constraints in multi-objective energy-noise wind farm layout optimization. Renew Energy 2016;85:359–70. https://doi.org/10.1016/j.renene.2015.06.026.
[6] Barthelmie RJ, Hansen KS, Frandsen ST, Rathmann O, Schepers JG, Schlez W, et al. Modelling and Measuring Flow and Wind Turbine Wakes in Large Wind Farms Offshore. Wind Energy 2009;12(5):431–44. https://doi.org/10.1002/we.348.
[7] Vermeer LJ, Sørensen JN, Crespo A. Wind turbine wake aerodynamics. Prog Aerosp Sci 2003;39(6-7):467–510. https://doi.org/10.1016/S0376-0421(03)00078-2.
[8] Jensen NO. A note on wind generator interaction. Tech rep. Roskilde (Denmark): Risø National Laboratory; 1983.
[9] Larsen GC. A simple wake calculation procedure. Tech rep. Roskilde (Denmark): Risø National Laboratory; 1988.
[10] Frandsen ST, Barthelmie RJ, Pryor SC, Rathmann O, Larsen S, Højstrup J, et al. Analytical modelling of wind speed deficit in large offshore wind farms. Wind Energy 2006;9(1–2):39–53. https://doi.org/10.1002/we.189.
[11] Katic I, Hojstrup J, Jensen NO. A simple model for cluster efficiency. In: Proceedings of the European wind energy conference and exhibition, Rome, Italy; 1986.
[12] Kuo JY, Romero DA, Amon CH. A mechanistic semi-empirical wake interaction model for wind farm layout optimization. Energy 2015;93:2157–65. https://doi.org/10.1016/j.energy.2015.10.009.
[13] Sanderse B, van der Pijl SP, Koren B. Review of computational fluid dynamics for wind turbine wake aerodynamics. Wind Energy 2011;14(7):799–819. https://doi.org/10.1002/we.458.
[14] Crespo A, Hernández J, Frandsen ST. Survey of modelling methods for wind turbine wakes and wind farms. Wind Energy 1999;2(1):1–24. https://doi.org/10.1002/(SICI)1099-1824(199901/03)2:1<1::AID-WE16>3.0.CO;2-7.
[15] Cabezón D, Migoya E, Crespo A. Comparison of turbulence models for the computational fluid dynamics simulation of wind turbine wakes in the atmospheric boundary layer. Wind Energy 2011;14(7):909–21. https://doi.org/10.1002/we.516.
[16] Antonini EGA, Romero DA, Amon CH. Analysis and modifications of turbulence models for wind turbine wake simulations in atmospheric boundary layers. In: Proceedings of the ASME 2016 international mechanical engineering congress & exposition, Phoenix, Arizona, USA; 2016. https://doi.org/10.1115/IMECE2016-67353.
[17] Antonini EGA, Romero DA, Amon CH. Analysis and modifications of turbulence models for wind turbine wake simulations in atmospheric boundary layers. J Sol Energy Eng 2018;140(3):031007. https://doi.org/10.1115/1.4039377.
[18] Mehta D, van Zuijlen AH, Koren B, Holierhoek JG, Bijl H. Large eddy simulation of wind farm aerodynamics: a review. J Wind Eng Ind Aerodyn 2014;133:1–17. https://doi.org/10.1016/j.jweia.2014.07.002.
[19] Shakoor R, Hassan MY, Raheem A, Wu YK. Wake effect modeling: a review of wind farm layout optimization using Jensen's model. Renew Sustain Energy Rev 2016;58:1048–59. https://doi.org/10.1016/j.rser.2015.12.229.
[20] Mosetti G, Poloni C, Diviacco D. Optimization of wind turbine positioning in large wind farms by means of a genetic algorithm. J Wind Eng Ind Aerodyn 1994;51(1):105–16. https://doi.org/10.1016/0167-6105(94)90080-9.
[21] Grady SA, Hussaini MY, Abdullah MM. Placement of wind turbines using genetic algorithms. Renew Energy 2005;30(2):259–70. https://doi.org/10.1016/j.renene.2004.05.007.
[22] Kusiak A, Song Z. Design of wind farm layout for maximum wind energy capture. Renew Energy 2010;35(3):685–94. https://doi.org/10.1016/j.renene.2009.08.019.
[23] Serrano González J, Gonzalez Rodriguez AG, Castro Mora J, Riquelme Santos JM, Burgos Payán M. Optimization of wind farm turbines layout using an evolutive algorithm. Renew Energy 2010;35(8):1671–81. https://doi.org/10.1016/j.renene.2010.01.010.
[24] Emami A, Noghreh P. New approach on optimization in placement of wind turbines within wind farm by genetic algorithms. Renew Energy 2010;35(7):1559–64. https://doi.org/10.1016/j.renene.2009.11.026.
[25] Chowdhury S, Zhang J, Messac A, Castillo L. Unrestricted wind farm layout optimization (UWFLO): Investigating key factors influencing the maximum power generation. Renew Energy 2012;38(1):16–30. https://doi.org/10.1016/j.renene.2011.06.033.
[26] Pookpunt S, Ongsakul W. Optimal placement of wind turbines within wind farm using binary particle swarm optimization with time-varying acceleration coefficients. Renew Energy 2013;55:266–76. https://doi.org/10.1016/j.renene.2012.12.005.

[27] Hou P, Hu W, Soltani M, Chen Z. Optimized placement of wind turbines in large-scale offshore wind farm using particle swarm optimization algorithm. IEEE Trans Sustain Energy 2015;6(4):1272–82. https://doi.org/10.1109/TSTE.2015.2429912.
[28] Hou P, Hu W, Chen C, Soltani M, Chen Z. Optimization of offshore wind farm layout in restricted zones. Energy 2016;113:487–96. https://doi.org/10.1016/j.energy.2016.07.062.
[29] Hou P, Hu W, Soltani M, Chen C, Chen Z. Combined optimization for offshore wind turbine micro siting. Appl Energy 2017;189:271–82. https://doi.org/10.1016/j.apenergy.2016.11.083.
[30] Bilbao M, Alba E. Simulated annealing for optimization of wind farm annual profit. In: Prooceedings of the 2nd international symposium on logistics and industrial informatics, Linz, Austria; 2009. p. 1–5. https://doi.org/10.1109/LINDI.2009.5258656.
[31] Ozturk UA, Norman BA. Heuristic methods for wind energy conversion system positioning. Electr Power Syst Res 2004;70(3):179–85. https://doi.org/10.1016/j.epsr.2003.12.006.
[32] Du Pont BL, Cagan J. An extended pattern search approach to wind farm layout optimization. J Mech Des 2012;134(8):081002. https://doi.org/10.1115/1.4006997.
[33] Turner SDO, Romero DA, Zhang PY, Amon CH, Chan TCY. A new mathematical programming approach to optimize wind farm layouts. Renew Energy 2014;63:674–80. https://doi.org/10.1016/j.renene.2013.10.023.
[34] Feng J, Shen WZ. Solving the wind farm layout optimization problem using random search algorithm. Renew Energy 2015;78:182–92. https://doi.org/10.1016/j.renene.2015.01.005.
[35] Pérez B, Mínguez R, Guanche R. Offshore wind farm layout optimization using mathematical programming techniques. Renew Energy 2013;53:389–99. https://doi.org/10.1016/j.renene.2012.12.007.
[36] Guirguis D, Romero DA, Amon CH. Toward efficient optimization of wind farm layouts: utilizing exact gradient information. Appl Energy 2016;179:110–23. https://doi.org/10.1016/j.apenergy.2016.06.101.
[37] Thévenin D, Janiga G. Optimization and computational fluid dynamics. Springer; 2008.
[38] Kuo JY, Romero DA, Beck JC, Amon CH. Wind farm layout optimization on complex terrains Integrating a CFD wake model with mixed-integer programming. Appl Energy 2016;178:404–14. https://doi.org/10.1016/j.apenergy.2016.06.085.
[39] King RN, Hamlington PE, Dykes K, Graf P. Adjoint optimization of wind farm layouts for systems engineering analysis. In: Proceedings of the 34th wind energy symposium. https://doi.org/10.2514/6.2016-2199.
[40] King RN, Dykes K, Graf P, Hamlington PE. Optimization of wind plant layouts using an adjoint approach. Wind Energy Sci 2017;2(1):115–31. https://doi.org/10.5194/wes-2-115-2017.
[41] Giles MB, Pierce NA. An introduction to the adjoint approach to design. Flow, Turbul Combust 2000;65(3–4):393–415. https://doi.org/10.1023/a:1011430410075.
[42] Jameson A. Aerodynamic design via control theory. Sci Comput 1988;3(3):233–60. https://doi.org/10.1007/BF01061285.
[43] Anderson WK, Venkatakrishnan V. Aerodynamic design optimization on unstructured grids with a continuous adjoint formulation. Comput Fluids 1999;28(4–5):443–80. https://doi.org/10.1016/S0045-7930(98)00041-3.
[44] Plessix R-E. A review of the adjoint-state method for computing the gradient of a functional with geophysical applications. Geophys J Int 2006;167(2):495–503. https://doi.org/10.1111/j.1365-246X.2006.02978.x.
[45] Papadimitriou DI, Giannakoglou KC. A continuous adjoint method with objective function derivatives based on boundary integrals, for inviscid and viscous flows. Comput Fluids 2007;36(2):325–41. https://doi.org/10.1016/j.compfluid.2005.11.006.
[46] Othmer C. A continuous adjoint formulation for the computation of topological and surface sensitivities of ducted flow. Int J Numer Methods Fluids 2008;58(8):861–77. https://doi.org/10.1002/fld.1770.
[47] Jameson A, Shankaran S, Martinelli L. Continuous adjoint method for unstructured grids. AIAA J 2008;46(5):1226–40. https://doi.org/10.2514/1.25362.
[48] Sørensen JN, Myken A. Unsteady actuator disc model for horizontal axis wind turbines. J Wind Eng Ind Aerodyn 1992;39(1–3):139–49. https://doi.org/10.1016/0167-6105(92)90540-Q.
[49] Ammara I, Leclerc C, Masson C. A viscous three-dimensional differential/actuator-disk method for the aerodynamic analysis of wind farms. J Sol Energy Eng 2002;124(4):345. https://doi.org/10.1115/1.1510870.
[50] Dwight RP, Brezillon J. Effect of approximations of the discrete adjoint on gradient-based optimization. AIAA J 2006;44(12):3022–31. https://doi.org/10.2514/1.21744.
[51] Castro C, Lozano C, Palacios F, Zuazua E. Systematic continuous adjoint approach to viscous aerodynamic design on unstructured grids. AIAA J 2007;45(9):2125–39. https://doi.org/10.2514/1.24859.
[52] The OpenFOAM Foundation Ltd. OpenFOAM 2.4.0. < http://www.openfoam.org/ > [accessed: June 2016].
[53] Weller HG, Tabor G, Jasak H, Fureby C. A tensorial approach to computational continuum mechanics using object-oriented techniques. Comput Phys 1998;12(6):620. https://doi.org/10.1063/1.168744.
[54] Stück A. Adjoint Navier-Stokes methods for hydrodynamic shape optimisation [Ph.D. thesis]. Technischen Universität Hamburg; 2012.
[55] Kraft D. A software package for sequential quadratic programming. Tech rep. Germany: Institut für Dynamik der Flugsysteme, Oberpfaffenhofen; 1988.
[56] Johnson SG. The NLopt nonlinear-optimization package. < http://ab-initio.mit.edu/nlopt > [accessed: June 2016].
[57] Loken C, Gruner D, Groer L, Peltier R, Bunn N, Craig M, et al. SciNet: lessons learned from building a power-efficient top-20 system and data centre. J Phys: Conf Ser 256(1). https://doi.org/10.1088/1742-6596/256/1/012026.